Journal of Zhejiang University-SCIENCE A (Applied Physics & Engineering)
ISSN 1673-565X (Print); ISSN 1862-1775 (Online)
www.jzus.zju.edu.cn; www.springerlink.com
E-mail: jzus@zju.edu.cn

Fabrication and performance analyses of 45# steel supports using liquid forging*

Yong-gen SUN[†1,2], Yu-shi QI[2], Jiao LI[2], Zhi-ming DU[†‡1], Li-li CHEN[2], Li-hua CHEN[3]

[1]*National Key Laboratory for Precision Hot Processing of Metals, Harbin Institute of Technology, Harbin 150001, China*

[2]*School of Materials Science and Engineering, Harbin Institute of Technology, Harbin 150001, China*

[3]*Beijing North Vehicle Group Co. Ltd., Beijing 100072, China*

[†]E-mail: hitsunyg@163.com; duzm@263.net

Received Jan. 9, 2020; Revision accepted May 2, 2020; Crosschecked Oct. 28, 2020

Abstract: In this paper, 45# steel supports prepared by liquid forging showed excellent performances and the effects of processing techniques on the development of microstructures and mechanical properties of these steel supports were researched. The liquid forging process was simulated and technological parameters were optimized via a ProCAST simulation software. The solidification time, temperature distribution, first principal stress distribution of the 45# steel supports varied with time, temperatures, and position. Two principal parameters, pouring temperature and dwell time, were assessed for their effects on microstructures, mechanical properties, and wear resistance properties of 45# steel supports. Results showed that the optimal pouring temperature of the molten metal and the pressure-holding time were between 1540 °C and 1560 °C and between 35 s and 40 s, respectively. The microstructure, mechanical properties, and fracture behavior of different positions in the support were also discussed, and the central position performed better than the edge because of plastic deformation. Finally, the dynamic solidification process was also investigated and the liquid forging process of 45# steel supports was complex and contained some special metal liquid convection and several plastic deformation stages.

Key words: 45# steel; Liquid forging; Numerical simulation; Mechanical properties; Wear resistance; Fracture behavior
https://doi.org/10.1631/jzus.A2000012 **CLC number:** TG31

1 Introduction

Steel materials exhibit a number of outstanding performance characteristics including excellent mechanical properties, low production cost, high recovery rate, and abundant raw resources (Dong et al., 2017; Linz et al., 2017; Gao et al., 2019). Alongside the rapid development of the materials industry, however, no other material is able to completely replace steel materials. The steel materials are likely to remain the most important structural materials (Liu et al., 2010; Escobar et al., 2016; Qin et al., 2018). Cast forming (Li et al., 2018; Niu R et al., 2018) and liquid forging processes (Püttgen et al., 2007; Hirt et al., 2009; Rogal and Dutkiewicz, 2012) are common methods for fabricating steel parts. However, casting technology presents numerous technical drawbacks, including low automation levels and difficulty to control production process; this approach therefore results in poor steel part performance and restricts the wide application of materials (Mitchell, 1997; Song et al., 2019). Products formed by the liquid forging processes are able to overcome defect problems; for this reason, liquid forged steel is widely used in the automotive industry, for military supplies, and in aerospace technology (Murali and Yong, 2010; Li et al., 2011).

‡ Corresponding author
* Project supported by the International Cooperation Project of the Ministry of Science and Technology of China (No. 2014DFR50320) and the National Natural Science Foundation of China (No. 51174064)
ORCID: Yong-gen SUN, https://orcid.org/0000-0002-5147-3428

Combining casting and forging, liquid forging is a metal forming process that contains three stages, mold preparation and metal liquid pouring, mold clamping and pressing, as well as mold opening and demolding (Bi et al., 2010). During the forming process, the metal liquid is poured into an open die and a punch moves down to pressurize the metal liquid. A blank or part, with precise dimensions, is then created through the solidification and shrinkage of metal liquid under applied pressure. Previous studies showed that the forming process can significantly improve production efficiency, enhance product performance, and reduce material loss (Cheng et al., 2010; Li et al., 2013).

The process of liquid forging is relatively complex, however, as it encompasses fluidics, heat conduction, and some plastic deformation (Zheng et al., 2015; Fang et al., 2016). During the final stage of the process, defects such as hot cracking and shrinkage cavities will occur due to inward stress when the metal molten temperature falls to within the brittle temperature range (Li et al., 1992; Du et al., 2011; Sosenushkin et al., 2015) and seriously influences the properties of formed parts. It is of vital importance in the development of liquid forging technology to fabricate the liquid-forged steel parts with excellent properties by optimizing process parameters, reducing production cost, and shortening production cycle.

The aim of this study was to address the fabrication of 45# steel supports for liquid forging under different process conditions in order to develop enhanced mechanical properties. Pouring temperature and dwell time were investigated in terms of how they influence the microstructure and mechanical properties of liquid forging parts. Simulation software was adopted to simulate the forming process. The performances of different positions in the support were researched. The forming parameters were further optimized, and the 45# steel parts with good properties were fabricated. The dynamic solidification process was also discussed to establish a theory for the liquid forging of steel.

2 Experimental

The experimental material used here was 45# steel (Dongbei Special Steel Group Co. Ltd., Harbin, China). The chemical composition of 45# steel was measured using an X-ray fluorescence spectrometer (AXIOS-PW4400, Malvern Panalytical, Almelo, the Netherlands), as shown in Table 1. The thermal properties of experimental 45# steel samples were measured using a synchronous thermal analyzer (TGA/SDTA851e, Mettler Toledo, Zurich, Switzerland). The differential scanning calorimetry (DSC) results recovered here are shown in Fig. 1a; these demonstrate that the liquidus temperature is 1495 °C and the solidus temperature is 1450 °C. The liquid-phase ratio of 45# steel at different temperatures is as shown in Fig. 1b.

Table 1 Chemical composition of 45# steel

Composition	Content (%, in weight)	Composition	Content (%, in weight)
Fe	98.316	Cu	≤0.25
C	0.42–0.50	Cr	≤0.25
Si	0.17–0.37	Mn	0.5–0.8
Ni	≤0.25		

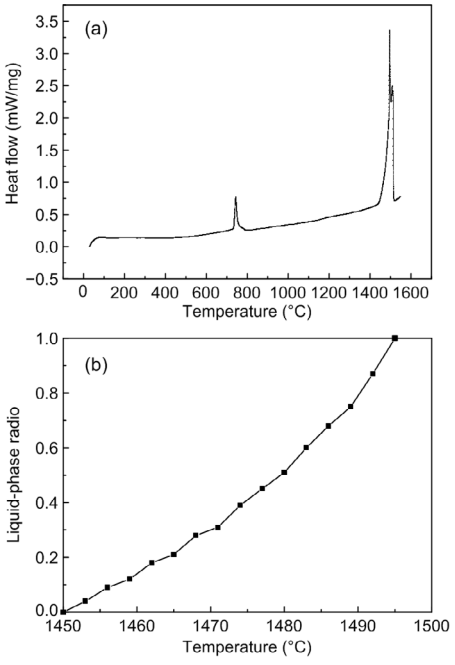

Fig. 1 DSC curve (a) and variation of the liquid fraction (b) of 45# steel with temperature

The ProCAST simulation software is a commercially available finite element modeling package for foundry and casting simulations for analysis of investment casting based on a variety of components. This software was employed to simulate the process of liquid forging forming. Variations in temperature

and stress fields during the forming process were analyzed.

Block 45# steel samples were cut to dimensions of 50 mm×50 mm×50 mm. Each surface was then de-rusted and ultrasonically cleaned in acetone for approximately 10 min. The prepared samples were then placed in a 45-kW medium frequency induction furnace (CW-MF-45, Kunshan Zhenlin Industrial Co. Ltd., Kunshan, China) and heated to melt. The mold was preheated and the inner surface of the die was covered with zinc oxide and graphite; when the temperature of molten steel reached pouring temperature, liquid metal was decanted with a pouring ladle in order to decrease heat loss. A punch controlled with a hydro press (THP16-200, Tianjin No. 2 Forging Machine Tool Factory, Tianjin, China) was moved downwards to pressurize the molten steel with the maximum pressure and maintained this for a number of seconds. The punch then returned the stroke and the ejector rods ejected the forming part to complete the entire forming process. The flowchart of 45# steel support prepared by the liquid forging forming process is illustrated in Fig. 2, while Table 2 summarizes the experimental parameters.

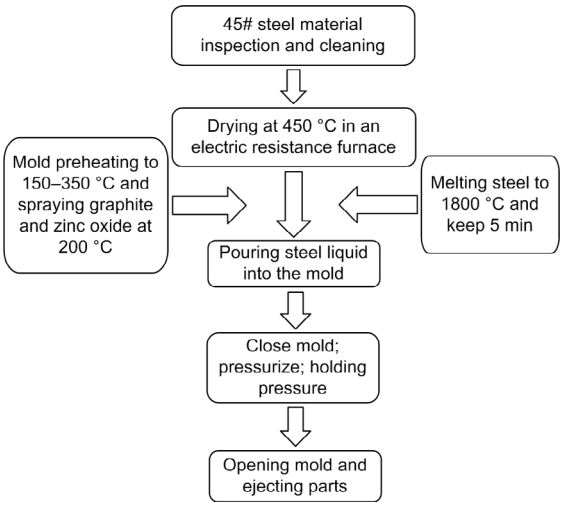

Fig. 2 Flow chart of 45# steel support liquid forging

The tensile test was performed in an electronic universal machine (AG-Xplus-250kN, Shimadzu Corporation, Kyoto, Japan) at room temperature. Vickers hardness was also measured using a Vickers hardness tester (310HVS-5, Wuxi Huayin Testing Instrument Sales Co., Ltd., Wuxi, China), and the Vickers hardness (HV) was calculated as follows:

$$\mathrm{HV}=\frac{P}{F}=\frac{2P\sin(136°/2)}{d^2}=1.8544\frac{P}{d^2}, \quad (1)$$

where P denotes the applied load, F is the indentation surface area, and d is the average length of the indentation diagonal line.

A friction and wear test was conducted on a pin-disk friction and wear tester (yТИТ13-100, Low Temperature Physics Institute, Ukraine) at air room temperature. Microstructures were observed using metallurgical microscopy (OLYMPUS-PEM-3, Hatagaya, Japan) while the microscopic morphology of fractures was observed using a scanning electron microscope (Zeiss Merlin Compact, Carl Zeiss, Jena, Germany).

Table 2 Test process parameters

Number	Pouring temperature (°C)	Mold temperature (°C)	Holding time (s)
1	1500	350	35
2	1520	350	35
3	1540	350	35
4	1560	350	35
5	1580	350	35
6	1540	350	25
7	1540	350	30
8	1540	350	35
9	1540	350	40
10	1540	350	45

3 Results and discussion

3.1 Simulation analysis of 45# steel support liquid forging

Fig. 3a illustrates the total solidification time in the simulation at different mold preheating temperatures. Results show that solidification time of the 45# steel part increases with increasing mold preheating temperature due to the decreasing difference between the liquid metal and the mold. Thus, when the metal liquid pouring temperature was 1540 °C and the forming pressure was 100 MPa, solidification time increased from 31.6 s at a mold preheating temperature of 150 °C to 38.3 s at a mold preheating temperature of 350 °C. Solidification time was also influenced by pouring temperature. As the pouring temperature of the molten metal was elevated, the solidification time of the forming parts gradually increased

(Fig. 3b). This means that the solidification shrinkage of the inner metal liquid at a higher temperature is hindered by the solidified metal shell at the outer layer. Pressure exerts a significant influence on the forming and solidification process of the forming parts (Fig. 3c); solidification time decreased from 67.3 s under a forming pressure of 0.1 MPa to 35.0 s under 150 MPa as the metal liquid pouring temperature was 1540 °C and the mold preheating temperature was 300 °C. The pressure of the metal liquid affected boundary conditions between the forming part and the mold, and the heat transfer coefficient increased with the increasing pressure. It resulted in the solidification time shortening. However, when the forming pressure was larger than 50 MPa, solidification time was basically stable with increasing pressure due to the limit of the heat transfer coefficient.

Fig. 4 shows the gradually variable solid fraction of the forming part at different times with a preheating temperature of 300 °C, a metal liquid pouring temperature of 1540 °C, and a forming pressure of 100 MPa. The gray area is the solid phase. The metal liquid solidified from outside to inside with a total solidification time of 34.7 s. The outer surface contacted with the mold sidewall solidified first and formed a hard shell (the gray area) due to the large temperature difference (Fig. 4a). As time progressed, the shell became thick, the gray area expanded, and the solid phase increased (Figs. 4b and 4c). The upper part was fully coagulated while some latent heat remained in the lower area when solidification was conducted as shown in Fig. 4e. The summary in Figs. 4d–4f illustrates that the final solidification zone of the molten metal is in the lower center, likely to

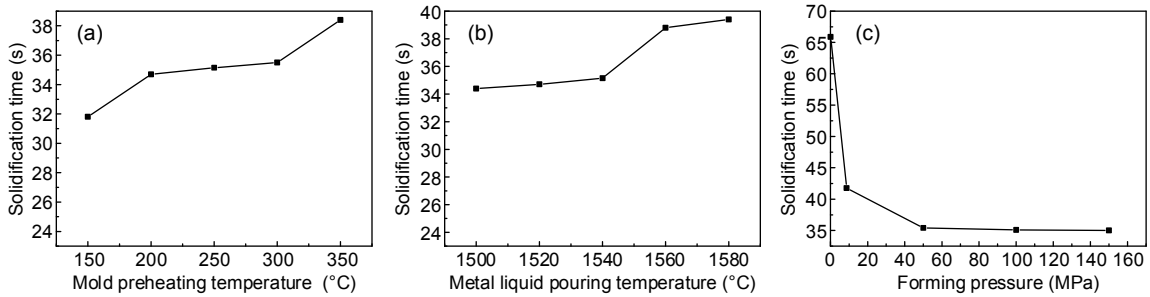

Fig. 3 Solidification time varies with mold preheating temperature (a), metal liquid pouring temperature (b), and forming pressure (c)

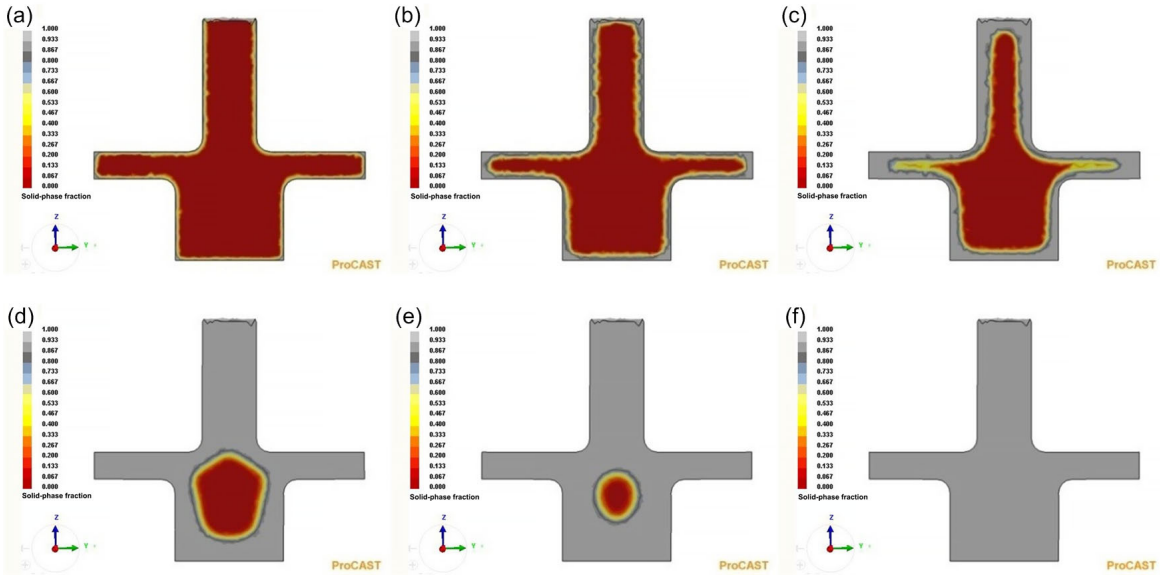

Fig. 4 Solid-phase fractions of the solidification process of support at different times: (a) t=0.8 s; (b) t=2.35 s; (c) t=5.0 s; (d) t=15.1 s; (e) t=25.1 s; (f) t=34.7 s

form a shrinkage cavity if the applied pressure is insufficient.

A total of eight sampling points were selected at different positions in the forming parts (Fig. 5a). Simulation parameters were then that the mold preheating temperature was 300 °C, the metal liquid pouring temperature was 1540 °C, and the forming pressure was 100 MPa. Fig. 5b shows the solid-phase fraction variation rule of each characteristic point with increasing time. The middle disc edge of the forming part solidified first, and then the rounded corners solidified. The heart area (point 5) solidified the slowest and there was almost no solidification in the first 25 s. This reached 80% in about 32 s and solidification was over with a 100% solid fraction after about 35 s. It was the case that each single characteristic area solidified rapidly, but the process only took about 10 s. The total solidification time was 35 s, always determined by final solidification area.

The temperature distribution of the forming part at different times was simulated at a preheating temperature of 300 °C, a pouring temperature of 1540 °C, and a pressure of 100 MPa (Fig. 6). The temperature of the contact position between the metal liquid and the mold surface decreased by 340 °C to about 1200 °C within 4.9 s (Fig. 6a), which was the fastest decrease across all positions. As time increased to 15.2 s, the temperature of this position fell quickly under 1000 °C (Fig. 6b), and the adjacent position began to cool rapidly (Fig. 6c). It is also worth

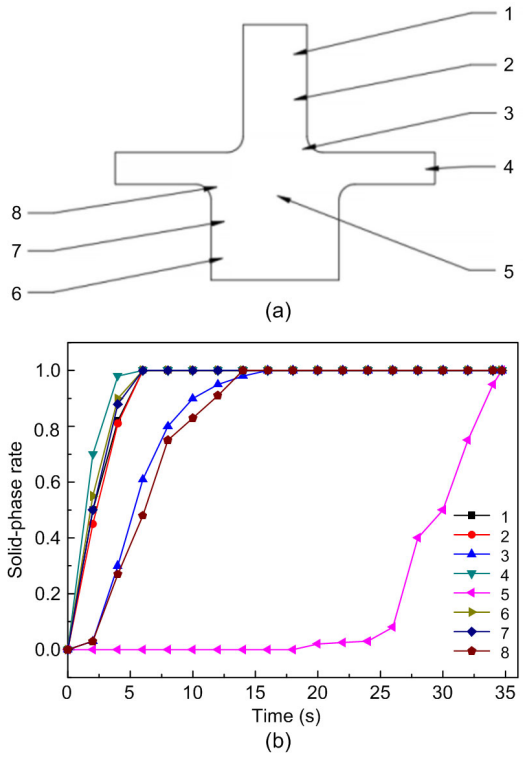

Fig. 5 Sampling positions of characteristic points (a) and solid fraction variation of characteristic points with time (b)

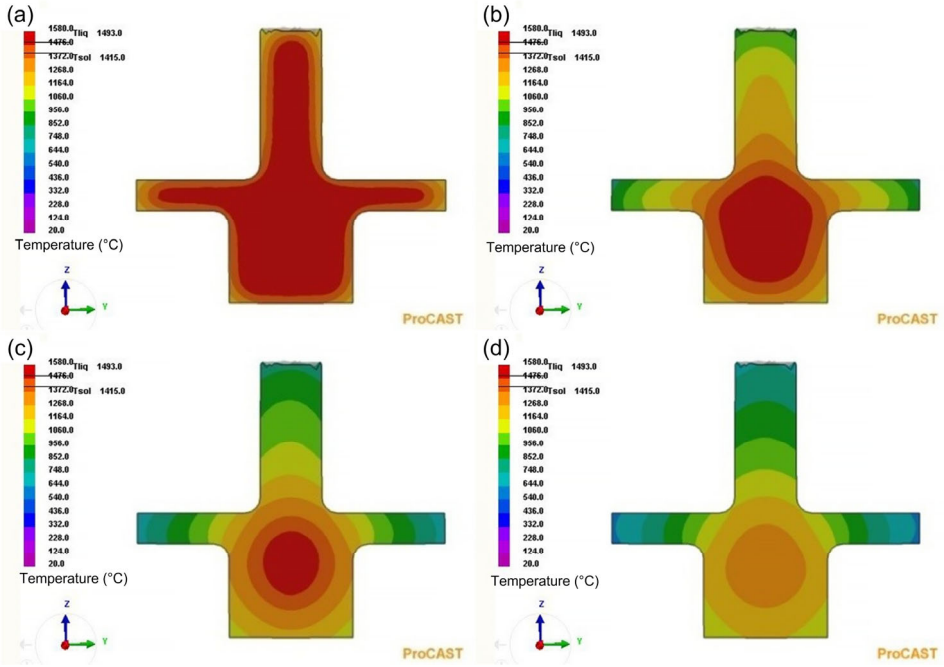

Fig. 6 Temperature distributions of forming part at different times: (a) t=4.9 s; (b) t=15.2 s; (c) t=25.2 s; (d) t=34.7 s

pointing out that the temperature at the center of the forming area is always higher than that of others, indicating that the center metal liquid solidifies last. This can be attributed to the pressure loss from the outside to the inside during the forming process, which results in a gradual increase of thermal resistance between the metal liquid and the mold. Although solidification was completed when after about 35 s, the temperature difference between the inside and the outside was still large. The temperature of the surface was about 600 °C, while the core temperature was about 1300 °C, as shown in Fig. 6d.

Fig. 7 illustrates the temperature change at characteristic points (Fig. 5) at different times with the mold preheating temperature of 300 °C, the pouring temperature of the metal liquid of 1540 °C, and the forming pressure of 100 MPa. These data show that the fastest temperature reduction occurs at the edge of the middle disc, and at the center it is the slowest. The temperature at the center was not only almost stable for the first 25 s but was also the highest.

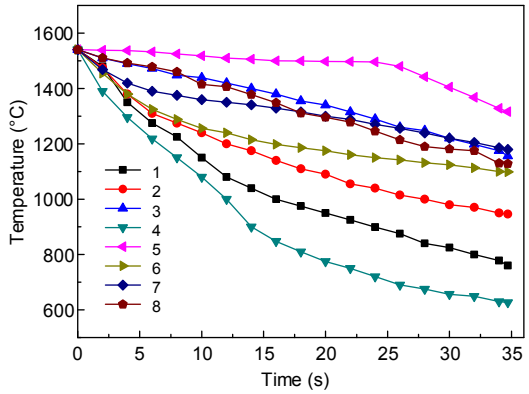

Fig. 7 Temperature variation at characteristic points with time

Fig. 8a shows the first principal stress distribution of each area during the solidification process with the mold preheating temperature of 300 °C, the pouring temperature of the molten metal of 1580 °C, and the applied pressure of 8.7 MPa. These data show that the stress value at the edge of the disc is much higher than that at the rounded corner or the center. Cracks were easily generated during solidification and shrinkage processes as the edge of the disc were obviously subjected to tensile stress. This was primarily because the metal liquid rapidly solidified and shrank on the outer surface as it contacted with the surface of the mold. Variation of the first principal stress with increasing time is shown in Fig. 8b; characteristic points within the forming area were all subjected to tensile stress due to solidification shrinkage. The edge of the disc was subject to the greatest stress, a dangerous area where crack defects were generated.

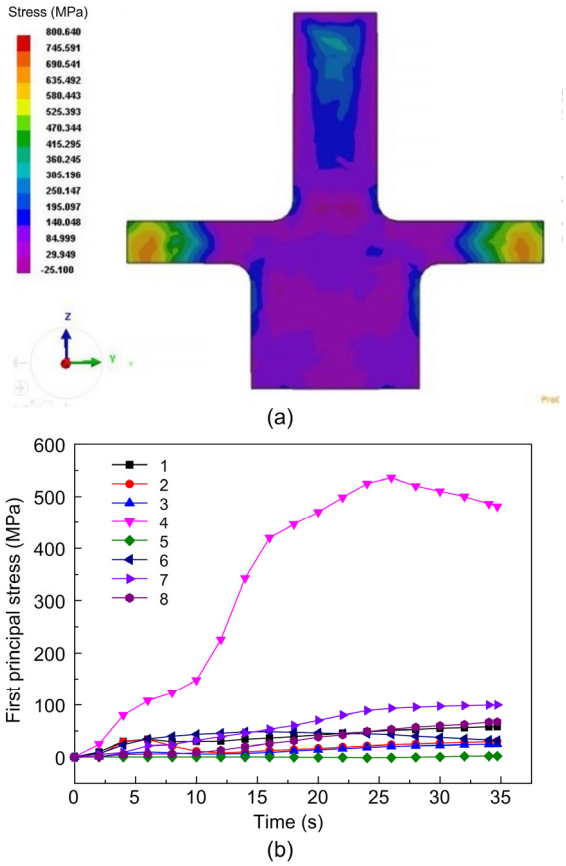

Fig. 8 First principal stress at different parts (a) and variation in first principal stress of the characteristic points with time (b)

3.2 Effect of pouring temperature on microstructure and 45# steel support properties

Simulation analysis results show that the edge of the 45# steel support solidified first and that the stress variation in this field was relatively complicated. Optical micrographs of the edge at different pouring temperatures were therefore observed when the dwell time was 35 s. Fig. 9 shows that when the pouring temperature is high and the cooling time is rapid, the microstructure of 45# steel due to liquid forging comprises pearlite and ferrite; the matrix is lamellar

pearlite while the white is net or granular ferrite. As the pouring temperature of the metal liquid increased, grain size decreased and then increased. Referring particularly to Figs. 9b–9d, the ferrite content increased and grains became coarse and inhomogeneous. Subsequent to the analysis, the effect of the pressure changed under increased pouring temperature; when the pouring temperature was below 1500 °C, thick crusts on the surface acted to hinder the transmission of pressure and grains remained relatively large. However, when the pouring temperature was 1540 °C, surface solidification time could better compensate for the delay time of pressure. The tight contact enlarged the interface heat transfer coefficient between the part and the mold, and grains were refined due to a large undercooling degree. However, when the pouring temperature was too high (1580 °C), dissociative grains formed by dendrite melting were saved, the internal crystal core decreased, and abnormal grain growth was seen. Severe carbon and silicon burned were also present because of excessive temperature in the solidification process. A large number of carbides were formed at high temperatures (Fig. 9e).

Combined with 45# steel components (Table 1), some parts exhibit better strength and plasticity as shown in Fig. 10. Fig. 10a illustrates the yield and tensile strength of the middle disc edge at different pouring temperatures. The yield sand tensile strengths were 315.4 MPa and 721.5 MPa, which were the lowest at a pouring temperature of 1500 °C, respectively. Indeed, as the pouring temperature increased, the yield strength was enhanced and had a tendency to stabilize, while the tensile strength initially increased but then dropped. These changes can be ascribed to inadequate pressure transmission and insufficient feeding of liquid metal because of low pouring temperature. As pouring temperature rose, the strength of forming parts was strengthened due to the improved feeding of molten metal and the ferrite content in the structure. The maximum yield strength was 349.9 MPa at a pouring temperature of 1560 °C, while the maximum tensile strength was 783.4 MPa at 1540 °C. It could be seen that the percentage of elongation increased at first and then decreased as pouring temperature increased (Fig. 10b). The lowest percentage of elongation was 16.1% at a pouring temperature of 1500 °C, while the highest was 17.1% at 1540 °C. The percentage of elongation value fluctuated within 1.0% at the experimental pouring temperature range. Mechanical properties of formed parts correspond to metallographic structures; when the pouring temperature was 1540 °C, metal liquid feeding was promoted. The ferrite and pearlite were evenly distributed in the structure and this resulted in a high percentage of elongation. The hardness at the edge at different pouring temperatures is shown in Fig. 10c; hardness performance is also connected to grain size and ferrite content. The maximum Vickers hardness was 242.7 at a pouring temperature of

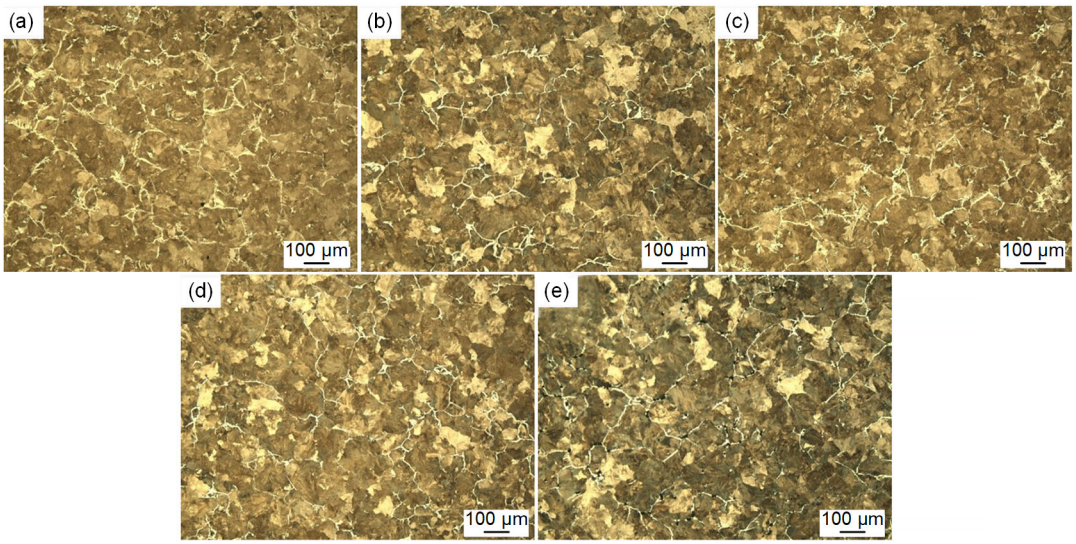

Fig. 9 Edge optical micrographs at different pouring temperatures: (a) 1500 °C; (b) 1520 °C; (c) 1540 °C; (d) 1560 °C; (e) 1580 °C

1540 °C; this hardness value decreased as pouring temperature increased. Similarly, Fig. 10d shows wear rate and specimen friction coefficient at different pouring temperatures. The wear rate was lower and the friction coefficient was elevated generally, which indicated that the wear resistance of liquid forged parts was significantly enhanced. As pouring temperature increased, wear rate fluctuated over a small range and the friction coefficient reached a maximum value of 0.38 at 1560 °C.

3.3 Effect of dwell time on microstructure and properties of 45# steel support

Edge optical micrographs under different pressure-holding times are shown in Fig. 11 when the pouring temperature was 1540 °C. It is observed that

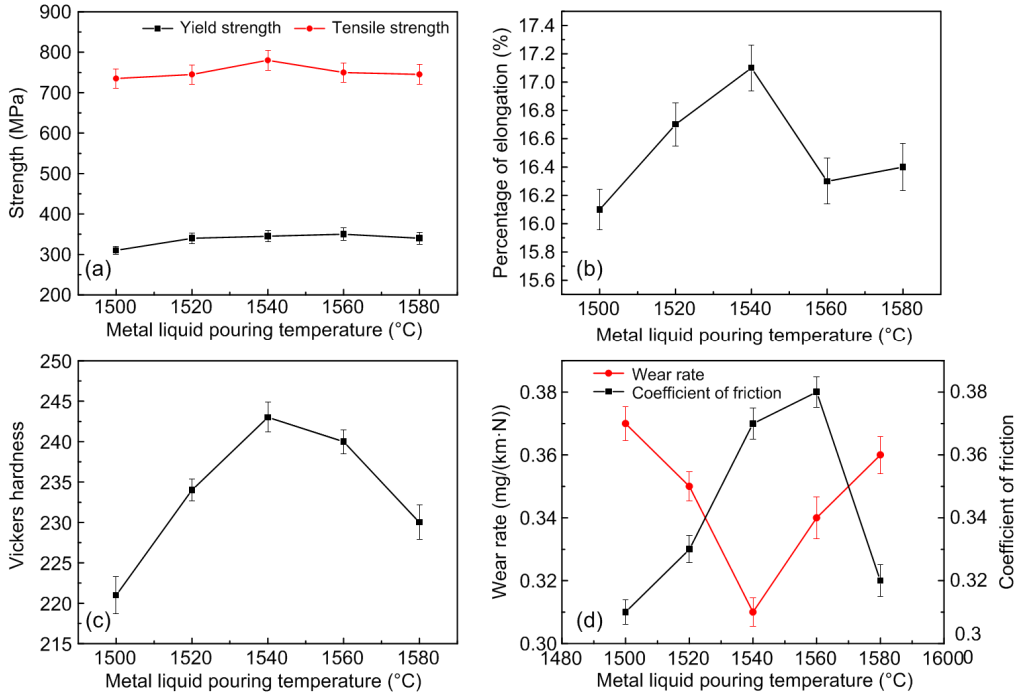

Fig. 10 Edge properties at different pouring temperatures: (a) strength; (b) percentage of elongation; (c) Vickers hardness; (d) wear rate

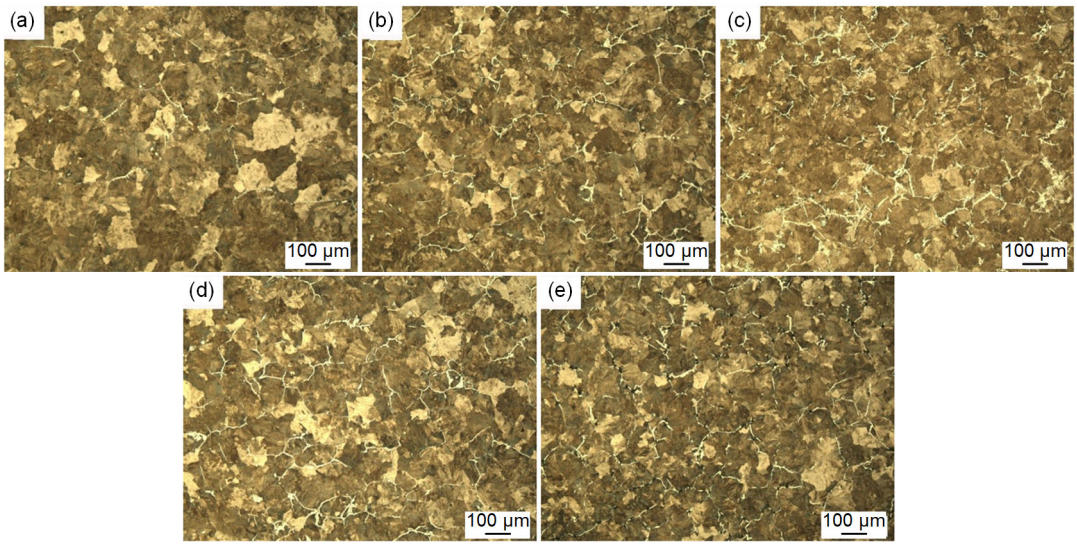

Fig. 11 Edge optical micrographs under different dwell times at 1540 °C: (a) 25 s; (b) 30 s; (c) 35 s; (d) 40 s; (e) 45 s

ferrite with unclear boundaries is unevenly distributed when the dwell time is short (25 s). One reason for this was that premature pressure was released and so the unsolidified metal liquid was not well compensated when it continually solidified. A few shrink holes also appeared. As pressure-holding time increased, the temperature distribution of forming parts tended to be uniform, the internal stress dropped, and the internal shrinkage defects disappeared. Ferrite content in the structure also increased, and pearlite grain size was reduced. Indeed, when dwell time was 35 s, strip ferrite distributed on the pearlite matrix could be seen and the grain distribution was uniform. Subsequently, as pressure-holding time was extended, the homogenization trends of structure and temperature were weak, and variations in grain size and grain distribution were not obvious.

Fig. 12 summarizes the mechanical performance of the edge under different dwell times with the pouring temperature of 1540 °C. Fig. 12a shows the yield and tensile strengths of the middle disc edge; the average yield and tensile strengths of the specimens are the lowest, 300.3 MPa and 720.1 MPa, respectively when the dwell time is 25 s. This was because feeding of liquid metal was insufficient over short times. However, as pressure-holding time increased, the strength of the forming part was enhanced. The maximum yield and tensile strengths are 343.1 MPa and 783.4 MPa, respectively, when the dwell time reaches 35 s. This can be attributed to the dense microstructure and increase in ferrite content. Subsequently, grains were displaced as dwell time increased, cooling shrinkage was limited, and strength was slightly reduced. Percentages of elongation of the edge data under different dwell times are shown in Fig. 12b; these demonstrate that the maximum percentage of elongation rate is 17.1% at 35 s. Indeed, when the dwell time was 35 s, unsolidified metal liquid was well-compensated and the shrink holes disappeared to form dense and uniform organization. All parts exhibited adequate toughness and strength. Fig. 12c indicates the edge hardness under different dwell times; these show that the Vickers hardness of the edge strengthened at first and then weakened as dwell time prolonged. Indeed, when dwell time was between 30 s and 40 s, Vickers hardness appeared stable. On the basis of plastic deformation strengthening theory (Tsuchiyama et al., 2016; Niu CN et al., 2018), forming parts deforms under certain specific pressures and reaches a certain density. This deformation cannot continue as deformation resistance increases. The density and mechanical properties will

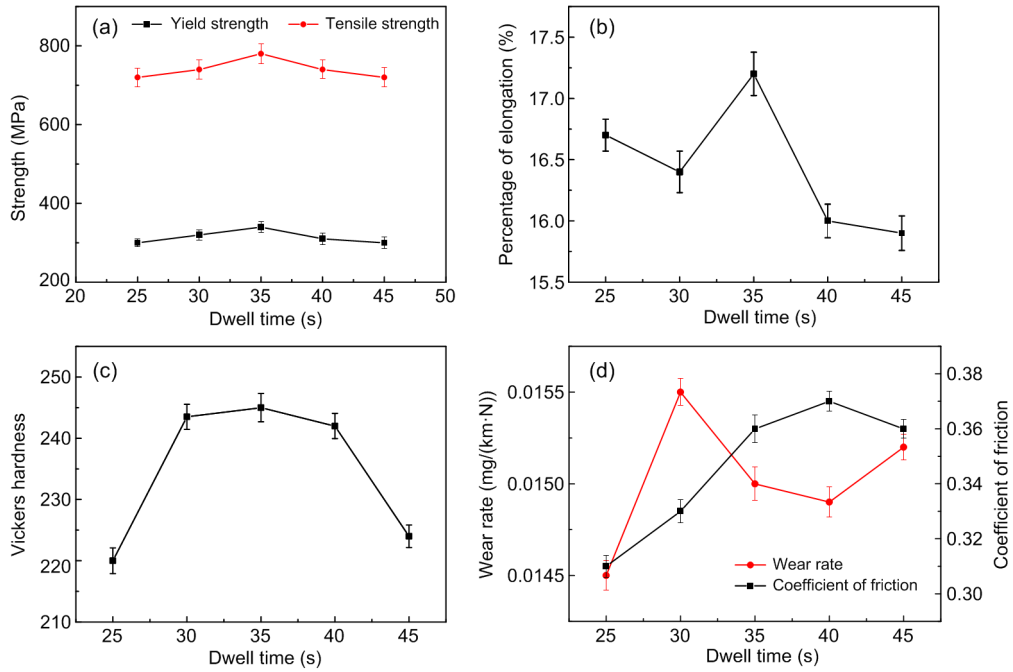

Fig. 12 Edge properties under different dwell times at 1540 °C: (a) strength; (b) percentage of elongation; (c) Vickers hardness; (d) wear rate

also not increase. Fig. 12d shows the wear rate and the friction coefficient of a sample at the middle disc edge under different pressure-holding times. The results show that as dwell time increases, the wear rate fluctuates within a small range under the dwell time between 30 s and 45 s. The friction coefficient first increased and then decreased, achieving a maximum value of 0.37 when the dwelling time was 40 s. When the dwell time was 35 s, the friction coefficient was 0.36. Combining these results with the microstructure of the specimen (Fig. 11), it is clear that grains grow and the microstructure is compacted gradually with increasing dwelling time. Although grains began to grow abnormally after 35 s, the organization of samples was denser at 40 s and wear properties were enhanced. It was also the case that when the dwelling time was 45 s, abnormal growth was very obvious and overall performance of parts was poor.

3.4 Microstructure and specimen properties at different positions

Different positions in the support were sampled (Fig. 13) where the pouring temperature was 1540 °C and the dwell time was 35 s. Optical micrographs of samples can be viewed in Fig. 14; widmanstatten structures were observed at position 1 (Fig. 14a) and position 2 (Fig. 14b) while needle ferrite precipitated along the original austenite grain boundary distributed on the pearlite. Grains remained relatively fine due to large plastic deformation in these positions during formation. The blocky ferrites located at the interval of pearlite at positions 3 and 4 are shown in Figs. 14c and 14d, respectively. The weak widmanstatten structures and finer grains with dense distribution could be observed at positions 5 and 6 as the organizations in these positions underwent plastic deformation.

The yield and tensile strengths at different positions (Fig. 15) are illustrated in Fig. 16a. Fig. 16 shows that the tensile strength of the edge is higher than that of the center. The central area was the last solidification zone of the metal liquid where shrinkage cavities easily formed when liquid metal feeding was insufficient. This corresponded to the optical

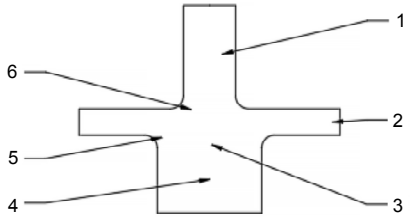

Fig. 13 Optical micrograph sampling positions

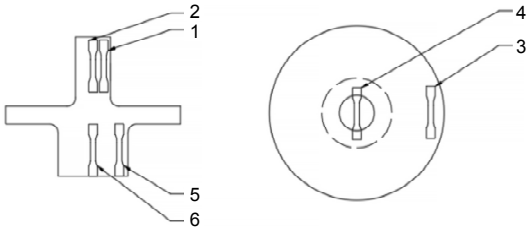

Fig. 15 Tensile test sampling positions

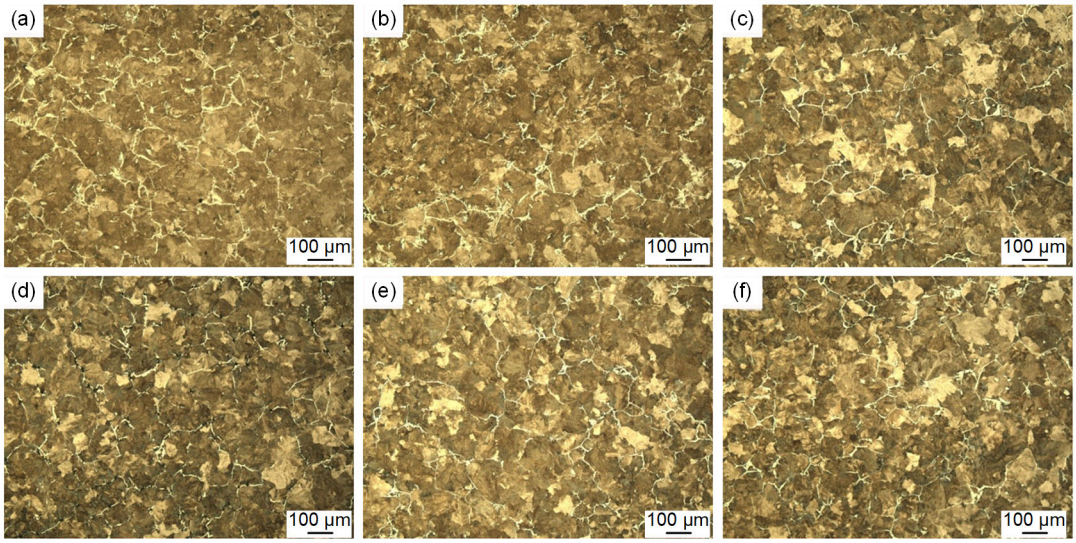

Fig. 14 Optical micrographs of different positions in the support: (a) position 1; (b) position 2; (c) position 3; (d) position 4; (e) position 5; (f) position 6

micrographs of the forming parts, and there were several shrinkage defects observed in the center of the parts. Fig. 16b illustrates the percentage of elongation at different positions. The percentage of elongation in the central position was higher than the one in the edge, while this variable in the central bottom (position 6) rose up to 22.1%. The Vickers hardness of position 1 was 251.3, the highest in Fig. 16c. This can be attributed to the three-direction compressive stress that results in large deformation. The solidification and shrinkage of the metal liquid in the center (position 3) was hindered by solidified metal in the outer layer and tensile stress was generated. The Vickers hardness at position 3 was the lowest (230.1). The wear rate and friction coefficients at different positions are shown in Fig. 16d. The wear rate at position 3 was higher than others and the friction coefficient at position 2 was the largest because of large plastic deformation. Several internal shrinkage defects also exist in the center; the friction coefficient of the center was lower than that of the edge and the round corner. Wear rate and wear resistance of the liquid forged forming parts were significantly improved.

Fig. 17 shows fracture morphology graphs of tensile specimens. The crystalline steps are seen in Figs. 17a and 17b where the fracture is brittle while Fig. 17c demonstrates pseudo-cleavage and dimple fracture where few tearing ridges are present on the fracture due to plastic deformation. A large number of equiaxial deep dimples and microscopic holes can also be observed in Fig. 17d; a cleavage fracture with river patterns and some small and shallow dimples is illustrated in Fig. 17e, indicating ductile fracture. Fig. 17f demonstrates a ductile intergranular fracture with a large number of slight dimples.

Results show that the toughness properties at positions 1 and 2 were relatively poor, as the fracture mainly brittle. In contrast, positions 4 and 6 had better toughness because of some plastic deformation in the forming process. All the two positions were the ductile fracture. Indeed, when the sample was stretched and deformed to a certain extent, some micro-holes formed. These micro-holes nucleated at the center of the neck with the smallest cross-sectional area and then gradually formed cracks as deformation behavior progressed (Viola et al., 2015; Morin et al., 2018). As these cracks approached the free surface of the forming part, the outer metal underwent plastic deformation and cracks began to become unstable and expanded rapidly.

3.5 Dynamic solidification process

Fig. 18 illustrates the dynamic solidification process of liquid forged 45# steel supports. Throughout the pouring process, metal liquid contacting the die wall rapidly cooled forming a hard,

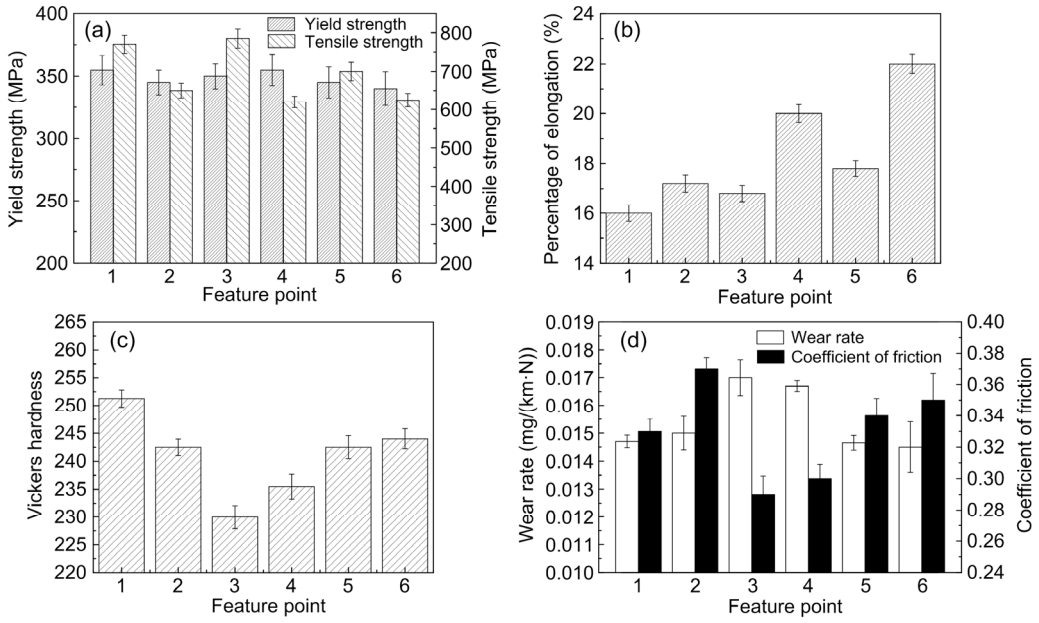

Fig. 16 Properties of different support positions: (a) strength; (b) percentage of elongation; (c) Vickers hardness; (d) wear rate

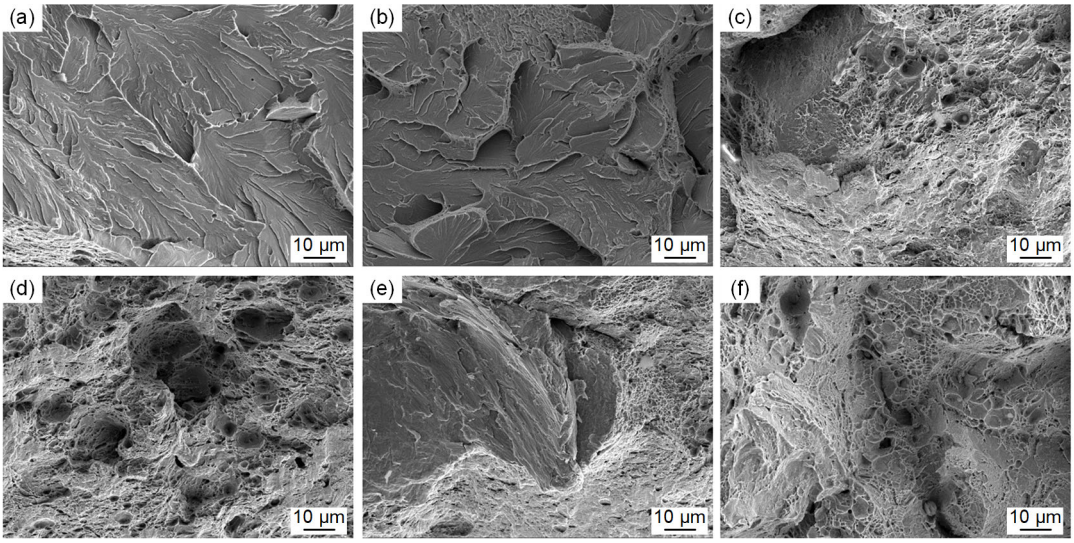

Fig. 17 Fracture morphology graphs of tensile specimens at different positions: (a) position 1; (b) position 2; (c) position 3; (d) position 4; (e) position 5; (f) position 6

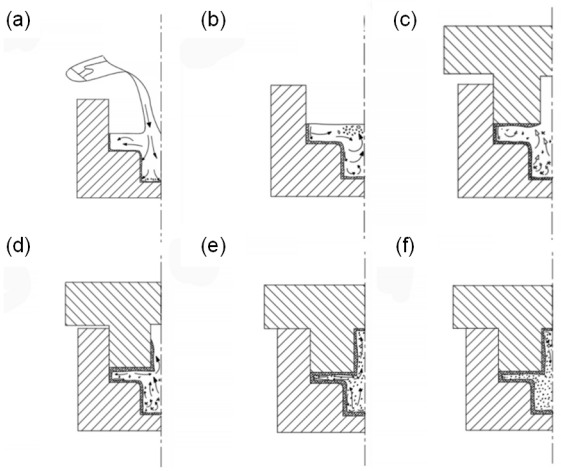

Fig. 18 Schematic of the liquid forged forming process of 45# steel supports: (a) mechanical scouring; (b) free convection of metal liquid; (c) complex free convection; (d) inter-dendritic convection; (e) plastic deformation; (f) reverse convection

shell layer because of the large temperature difference between the molten steel and the die wall. Due to metal liquid scouring, some agglomerates with weak crusts were fused and dissociated in the steel liquid (Fig. 18a), a process which inhibited the growth of columnar crystals. As internal liquid viscosity was low, free convection of the metal liquid occurred due to the density difference. Figs. 18b and 18c show free convection of the metal liquid before squeezing and complex free convection, respectively. As the punch affected the temperature distribution of the steel liquid when it went down, metal liquid reverse convection under this pressure is also shown (Fig. 18d). Steel liquid generated a strong flow in the variable cross-sectional cavity formed by the die and the punch. The unstable crystal blocks solidified first were stripped by severe reverse scouring. Thus, the punch contacted completely the metal liquid which then underwent convection in reverse under pressure as shown in Fig. 18e. As the punch went down, a thin shell layer formed on the steel liquid surface deformed in height and diameter. Fig. 18f demonstrates metal liquid inter-dendritic convection which continues until the steel liquid is completely solidified. As the metal liquid crystallized, low melting point phases with hot spots were transferred and accumulated at the final solidified position, resulting in macroscopic segregation (Guo et al., 2013; Ma and Li, 2016).

Dendrites in the liquid were fused and dissociated in the liquid under certain mechanical disturbances, significant features of liquid forging solidification (Bratu et al., 2014). The main processes here comprised the mechanical scouring of metal liquid during pouring, free, and reverse convection of metal liquid before and after punch pressure, metal liquid inter-dendritic convection during plastic deformation of the hard shell, and the flow of low melting point phases.

4 Conclusions

A series of 45# steel supports with excellent performances were fabricated via liquid forging. Forming process parameters were then investigated using a numerical simulation with the ProCAST simulation software. Conclusions can be drawn as follows:

1. Optimal pouring temperature of the molten metal and pressure-holding time were between 1540 °C and 1560 °C and 35 s and 40 s, respectively.

2. 45# steel supports prepared by liquid forging at a pouring temperature of 1540 °C and dwell time of 35 s had the optimum combination of properties. Tensile strength, percentage of elongation, Vickers hardness, and friction coefficient of the middle disc edge were 783.4 MPa, 17.1%, 242.7, and 0.36, respectively.

3. Performance of different positions in the support did not vary significantly; the central position performed better than the edge because of plastic deformation.

4. The liquid forging process of 45# steel supports was complex and contained some special metal liquid convection and several plastic deformation stages. The properties of these supports are therefore excellent.

Contributors

Zhi-ming DU and Yong-gen SUN designed the research. Yu-shi QI and Jiao LI processed the corresponding data. Yong-gen SUN wrote the first draft of the manuscript. Li-li CHEN and Li-hua CHEN helped to organize the manuscript. Yong-gen SUN and Zhi-ming DU revised and edited the final version.

Conflict of interest

Yong-gen SUN, Yu-shi QI, Jiao LI, Zhi-ming DU, Li-li CHEN, and Li-hua CHEN declare that they have no conflict of interest.

References

Bi GJ, Ng GKL, Teh KM, et al., 2010. Feasibility study on the laser aided additive manufacturing of die inserts for liquid forging. *Materials & Design*, 31(S1):S112-S116. https://doi.org/10.1016/j.matdes.2009.10.039

Bratu V, Mortici C, Oros C, et al., 2014. Mathematical model of solidification process in steel continuous casting taking into account the convective heat transfer at liquid-solid interface. *Computational Materials Science*, 94:2-7. https://doi.org/10.1016/j.commatsci.2013.12.033

Cheng YS, Zhang YY, Du ZM, 2010. Liquid forging integral forming technology for aluminum matrix composites with local reinforcement. *Special Casting & Nonferrous Alloys*, 30(3):231-233 (in Chinese).

Dong J, Li C, Liu CX, et al., 2017. Hot deformation behavior and microstructural evolution of Nb-V-Ti microalloyed ultra-high strength steel. *Journal of Materials Research*, 32(19):3777-3787. https://doi.org/10.1557/jmr.2017.365

Du ZM, Chen G, Han F, et al., 2011. Homogenization on microstructure and mechanical properties of 2A50 aluminum alloy prepared by liquid forging. *Transactions of Nonferrous Metals Society of China*, 21(11):2384-2390. https://doi.org/10.1016/S1003-6326(11)61024-8

Escobar DP, de Dafé SSF, Verbeken K, et al., 2016. Effect of the cold rolling reduction on the microstructural characteristics and mechanical behavior of a 0.06%C-17%Mn TRIP/TWIP steel. *Steel Research International*, 87(1):95-106. https://doi.org/10.1002/srin.201400555

Fang XG, Lü SL, Zhao L, et al., 2016. Microstructure and mechanical properties of a novel Mg-RE-Zn-Y alloy fabricated by Rheo-Squeeze casting. *Materials & Design*, 94:353-359. https://doi.org/10.1016/j.matdes.2016.01.063

Gao B, Chen XF, Pan ZY, et al., 2019. A high-strength heterogeneous structural dual-phase steel. *Journal of Materials Science*, 54(19):12898-12910. https://doi.org/10.1007/s10853-019-03785-1

Guo J, Liu LG, Li Q, et al., 2013. Characterization on carbide of a novel steel for cold work roll during solidification process. *Materials Characterization*, 79:100-109. https://doi.org/10.1016/j.matchar.2013.02.011

Hirt G, Khizhnyakova L, Baadjou R, et al., 2009. Semi-solid forming of aluminium and steel-introduction and overview. *In*: Hirt G, Kopp R (Eds.), Thixoforming: Semi-solid Metal Processing. Wiley-VCH Verlag GmbH & Co. KGaA, New York, USA, p.1-27. https://doi.org/10.1002/9783527623969.ch1

Li HJ, Luo SJ, Qi LH, 1992. The stress states of a workpiece in the process of liquid-metal forging. *Journal of Materials Processing Technology*, 30(3):287-296. https://doi.org/10.1016/0924-0136(92)90221-D

Li JY, Cheng GG, Li LY, et al., 2018. The formation mechanism of Mn-Al-O inclusions in Fe-Cr-Mn stainless steel during continuous casting. *Steel Research International*, 89(5):1700461. https://doi.org/10.1002/srin.201700461

Li N, Xing SM, Bao PW, 2013. Microstructure and mechanical properties of nodular cast iron produced by melted metal die forging process. *Journal of Iron and Steel Research*,

20(6):58-62.
https://doi.org/10.1016/S1006-706X(13)60112-0

Li SL, Sun WL, Wang HQ, et al., 2011. Study on microstructures and mechanical properties of AlSi9Cu3 aluminum alloy fabricated by liquid forging. *Advanced Materials Research*, 418-420:353-356.
https://doi.org/10.4028/www.scientific.net/amr.418-420.353

Linz M, Rodríguez Ripoll M, Gachot C, et al., 2017. On the competition between plastic deformation and material detachment in Ferritic/Pearlitic steel under boundary lubrication. *Wear*, 376-377:813-821.
https://doi.org/10.1016/j.wear.2017.01.095

Liu FB, Wang JD, Chen DR, et al., 2010. The cavitation erosion of the 45# carbon steels implanted with titanium and nitrogen. *Tribology Transactions*, 53(2):239-243.
https://doi.org/10.1080/10402000903226341

Ma XP, Li DZ, 2016. Multiscale discrete crystal growth in the solidification of 20SiMnMo5 steel. *Crystal Growth & Design*, 16(6):3163-3169.
https://doi.org/10.1021/acs.cgd.5b01804

Mitchell A, 1997. Melting, casting, and forging problems in titanium alloys. *JOM*, 49(6):40-42.
https://doi.org/10.1007/BF02914712

Morin D, Hopperstad OS, Benallal A, 2018. On the description of ductile fracture in metals by the strain localization theory. *International Journal of Fracture*, 209(1):27-51.
https://doi.org/10.1007/s10704-017-0236-9

Murali S, Yong MS, 2010. Liquid forging of thin Al-Si structures. *Journal of Materials Processing Technology*, 210(10):1276-1281.
https://doi.org/10.1016/j.jmatprotec.2010.03.014

Niu CN, LaRosa CR, Miao JS, et al., 2018. Magnetically-driven phase transformation strengthening in high entropy alloys. *Nature Communications*, 9(1):1363.
https://doi.org/10.1038/s41467-018-03846-0

Niu R, Li BK, Liu ZQ, et al., 2018. Melting of moving strip during steel strip feeding in continuous casting process. *Steel Research International*, 89(5):1700407.
https://doi.org/10.1002/srin.201700407

Püttgen W, Hallstedt B, Bleck W, et al., 2007. On the microstructure and properties of 100Cr6 steel processed in the semi-solid state. *Acta Materialia*, 55(19):6553-6560.
https://doi.org/10.1016/j.actamat.2007.08.010

Qin F, Feng W, Wu ST, 2018. Microstructure and Vickers-hardness of 20CrMnTiH steel during hot compression testing. *Ironmaking & Steelmaking*, 45(6):537-543.
https://doi.org/10.1080/03019233.2017.1297003

Rogal Ł, Dutkiewicz J, 2012. Effect of annealing on microstructure, phase composition and mechanical properties of thixo-cast 100Cr6 steel. *Materials Characterization*, 68:123-130.
https://doi.org/10.1016/j.matchar.2012.03.018

Song GW, Tama BA, Park J, et al., 2019. Temperature control optimization in a steel-making continuous casting process using a multimodal deep learning approach. *Steel Research International*, 90(12):1900321.
https://doi.org/10.1002/srin.201900321

Sosenushkin EN, Frantsuzova LS, Kozlova EM, 2015. Effect of pressure and temperature factors on the solidification of cast iron and its structure in liquid forging. *Metal Science and Heat Treatment*, 57(5-6):309-316.
https://doi.org/10.1007/s11041-015-9881-7

Tsuchiyama T, Yamamoto S, Hata S, et al., 2016. Plastic deformation and dissolution of ε-Cu particles by cold rolling in an over-aged particle dispersion strengthening Fe-2mass%Cu alloy. *Acta Materialia*, 113:48-55.
https://doi.org/10.1016/j.actamat.2016.03.018

Viola E, Marzani A, Fantuzzi N, 2015. Interaction effect of cracks on flutter and divergence instabilities of cracked beams under subtangential forces. *Engineering Fracture Mechanics*, 151:109-129.
https://doi.org/10.1016/j.engfracmech.2015.11.010

Zheng CK, Zhang WW, Zhang DT, et al., 2015. Low cycle fatigue behavior of T4-treated Al-Zn-Mg-Cu alloys prepared by squeeze casting and gravity die casting. *Transactions of Nonferrous Metals Society of China*, 25(11):3505-3514.
https://doi.org/10.1016/S1003-6326(15)63992-9

中文概要

题　目：45#钢支座的液态模锻制备工艺及组织性能分析

目　的：以 45#钢支座为典型制件对钢质液态模锻制备工艺过程进行分析与优化。研究不同工艺参数对制件组织性能的影响，对制件不同位置的组织性能进行探讨，优化和改善液态模锻钢制制件性能，为钢制制件的液态模锻制备提供理论依据。

创新点：1. 利用数值模拟软件模拟分析了钢质液态模锻工艺过程，为试验分析提供理论依据；2. 对制件不同位置的组织性能分析，探讨了塑性变形在液态模锻工艺过程中的影响。

方　法：1. 采用 ProCAST 模拟软件对 45#钢液态模锻的凝固过程、温度场及应力场的变化进行模拟（图 6~8），并对液态模锻工艺过程进行理论优化；2. 采用单一变量法，讨论浇注温度和保压时间对成型件的微观结构、机械性能和耐磨性的影响（图 9~12）；3. 研究成型制件不同位置的微观组织、力学性能和断裂行为（图 14，16 和 17），并讨论液态模锻工艺过程中塑性变形对制件组织性能的影响；4. 探讨分析 45#钢支座的动态成形工艺（图 18），并研究 45#钢的液态模锻整体工艺过程。

结　论：1. 熔融金属的最佳浇注温度和保压时间分别在1540~1560 °C 和 35~40 s。2. 在浇注温度为1540 °C 和保压时间为 35 s 时，液态锻造制备的45#钢支座具有最佳的组织性能；此时支座盘边缘的抗拉强度、伸长率、维氏硬度和摩擦系数分别为 783.4 MPa、17.1%、242.7 和 0.36。3. 45#钢支座不同位置的组织性能差异不大，但由于塑性变形的原因，中间位置的性能表现优于边缘位置。4. 45#钢支座的液态锻造工艺过程相对较复杂，包含不同的金属液对流和塑性变形；这些特殊的过程导致 45#钢支座的组织性能相对优异。

关键词：45#钢；液体锻造；数值模拟；力学性能；耐磨性；断裂行为